



Topology optimization for concurrent design of layer-wise graded lattice materials and structures



Huikai Zhang, Yaguang Wang, Zhan Kang*

State key Laboratory of Structural Analysis for Industrial Equipment, Dalian University of Technology, Dalian, 116024, China

ARTICLE INFO

Article history:

Received 20 October 2018

Revised 23 December 2018

Accepted 20 January 2019

Available online 6 March 2019

Keywords:

Topology optimization

Concurrent design

Layer-wise

Graded lattice

Structural coverage constraint

Average porosity constraint

ABSTRACT

Mechanical properties of hierarchical lattice structures depend not only on their overall shapes and topologies, but also on their microstructural configurations. This paper proposes a new method for concurrent topology optimization of structures composed of layer-wise graded lattice microstructures. Both macroscale design variables representing the distribution of different lattice materials and microscale design variables defining the topologies of the microstructural unit cells are to be simultaneously optimized. This formulation thus integrates the microstructure design into the structural design, instead of pursuing a grey macroscale design and then interpreting the intermediate densities into certain microstructures. The proposed method also enlarges the design space by allowing for graded microstructures. Two new design constraints, namely the structural coverage constraint and the average porosity constraint, are introduced into the proposed optimization formulation to reduce the complexity of the constraints in the layer-wise graded design. The macroscale and microscale designs are linked by using the Asymptotic homogenization method to compute the effective elastic properties of the microstructured materials. Numerical examples show validity of the proposed method. It is also found that layer-wise graded lattice structures outperform those with uniform lattice microstructures in terms of structural stiffness. Finite element simulations of constructed models of the optimized designs suggest that graded lattice structures exhibit higher buckling resistance and ultimate load bearing capacity than single-scale solid material structures or uniform lattice structures under the same material usage.

© 2019 Elsevier Ltd. All rights reserved.

1. Introduction

Artificially designed graded materials are characterized by continuous spatial variations of material properties along a specified direction (Birman & Byrd, 2007; Jha, Kant, & Singh, 2013). Such materials become popular in biomedical, optoelectronics, spacecraft, chemical, and mechanical engineering applications (Gupta & Talha, 2015). With the fast development of additive manufacturing technology, which has created unprecedented possibilities of fabricating complex microstructures of multiple materials, it becomes possible to incorporate lattice (aka. cellular) materials with graded microstructures into macrostructures (Lakes, 1987; Popovich et al., 2017). Indeed, such inhomogeneous microstructures can also be found in some biomaterials, such as bones and shells (Liu, Meyers, Zhang, & Ritchie, 2017). Complex lattice structures, e.g. metamaterials with negative Poisson's ratio or negative thermal expansion coefficient (Xu & Pasini, 2016), ultralight

* Corresponding author.

E-mail address: zhankang@dlut.edu.cn (Z. Kang).

micro-lattices (Schaebler et al., 2011), and optical metasurfaces (Yu & Capasso, 2014) have been implemented by additive manufacturing.

Lattice materials possess useful mechanical (low mass density and relatively high specific stiffness) and multiphasic properties (high porosity, energy absorption, acoustic and vibrational damping, and thermal management capabilities) (Deshpande, Ashby, & Fleck, 2001; Evans, Hutchinson, Fleck, Ashby, & Wadley, 2001), and therefore have been applied in many fields, including light-weight structures (Wei et al., 2018), optical (Hentschel, Schaferling, Duan, Giessen, & Liu, 2017) and mechanical metamaterials (Frenzel, Kadic, & Wegener, 2017; Xu & Pasini, 2016). In the mentioned studies, the microstructures have periodic layouts. Graded lattice microstructures are able to realize better stiffness and energy absorption capability than uniform lattice microstructures (Al-Saeid, Masood, Faizan-Ur-Rab, Alomarah, & Ponnusamy, 2018). However, up to now, their designs are mostly based on designers' intuition or trials-and-errors approaches, which may pose a limit on the design space. Therefore, it becomes highly desirable to seek a more rational computer aided method to achieve concurrent designs of macrostructures and their graded lattice materials.

Topology optimization (Bendsoe & Sigmund, 2003; Huang & Xie, 2010; Wang, Wang, & Guo, 2003) recasts a structural design problem into a mathematical programming problem. It has been used in design of aerospace vehicles (Aage, Andreassen, Lazarov, & Sigmund, 2017; Zhu, Zhang, & Xia, 2016), additive manufactured products (Liu et al., 2018; Wang & Kang, 2017), optical and acoustic metasurfaces (Callewaert, Velev, Kumar, Sahakian, & Aydin, 2018; He & Kang, 2018; Lin et al., 2018) and biomechanical structures (Zhao, Zhou, Feng, & Xie, 2018). In particular, in conjunction with the inverse homogenization method (Sigmund, 1994; Sigmund & Torquato, 1997), topology optimization has been used to design microstructures with various target properties, e.g. extreme metamaterials (Huang, Radman, & Xie, 2011; Sigmund & Torquato, 1997), negative Poisson's ratio materials (Vogiatzis, Chen, Wang, Li, & Wang, 2017; Wang, 2018; Watts & Tortorelli, 2017; Zhang, Luo, & Kang, 2018), and functional materials (Wang, Luo, Zhang, & Qin, 2016). It has also been extended to the design of functional graded materials composed of lattice microstructures (Radman, Huang, & Xie, 2014; Zhou & Li, 2008). Despite of these developments, how to integrate the design optimization of microstructures with structural design problems still needs further investigations.

Ideally, microstructural design should also take the loading and boundary conditions of the macrostructure into account. For this purpose, Rodrigues, Guedes, and Bendsoe (2002) and Coelho, Fernandes, Guedes, and Rodrigues (2008) proposed to interpret intermediate-density elements in the macrostructure as certain microstructures and produced meaningful two-scale structural and material designs through a double-loop strategy. Therein, the inner-loop (microstructural optimization) iterations were conducted at each macroscale finite element, which to some extent increases the computational cost. Another formulation known as porous anisotropic material penalization considers concurrent design of structures composed of uniform microstructures (Yan, Cheng, & Liu, 2008). It is worth noting that, despite that multi-scale topology optimization using microstructured materials usually cannot further improve structural stiffness as compared with that using homogeneous solid materials, the achieved designs may possess a higher capability of buckling resistance (Clausen, Aage, & Sigmund, 2016). Another side effect of lattice material structure design is that it can be used to alleviate the need of adding support materials (though self-supporting constraints were not explicitly considered) and thus may be generally more suitable for additive manufacturing as compared with conventional single-scale structural designs.

The concept of graded microstructures (see e.g. Attia, 2017; Ghayesh & Farokhi, 2017; Ghayesh, Farokhi, Gholipour, & Tavallaeinejad, 2018) has also been explored in topology optimization studies. Zhang and Sun, 2006 presented a multi-layer model, which assigned different microstructures to intermediate macroscale elements. This idea was extended to the concurrent design of two-scale structures (Li, Luo, Zhang, Gao, & Brown, 2016; Wang, Chen, & Wang, 2017). Wang et al. (2017) studied topology optimization of spatially varying graded microstructures, which can generate a series of similar graded microstructural topologies with different volume fractions. Li, Luo, Gao, and Walker (2018) implemented optimization of multi-layer and multi-patch graded lattice structures. These density-based works also interpret intermediate grey elements in the macrostructure as certain porous microstructures, and impose an individual volume fractions constraint to each type of microstructural unit cells.

This study aims to develop a new concurrent topology optimization formulation for graded multi-layer lattice structures. The macrostructure is first divided into a given number of layers in the specified direction. The topologies of the macroscale and microscale structures are respectively defined by macroscale and microscale design variables. In comparison with some other concurrent design methods that interpret grey elements into certain porous microstructures as a post-processing of the macroscale design, this study intends to separate the microstructure representation from the macrostructural layout description using independent microscale design variables. In order to drive the density values of macroscale elements to either 0 or 1, we employ the penalized interpolation model used in conventional SIMP method and introduce new design restrictions into the optimization model. To this end, we define a structural coverage constraint (SCC) to control the layouts of different microstructures, and an average porosity constraint (APC) to restrict the total material usage. This model not only reduces the computational cost in comparison with the design with point-wise different microstructures (Rodrigues et al., 2002; Zhu, Skouras, Chen, & Matusik, 2017), but also reduces the complexity of the microscale design constraints used in some previous studies, which impose volume constraints on each microstructure. We also show that the proposed method can be naturally extended to design optimization of multi-material hierarchical structures.

The remainder of this paper is organized as follows. In Section 2, design variables of the proposed two-scale optimization formulation are introduced, and the physical meanings of the structural coverage constraint and the average porosity constraint are discussed. Section 3 gives a brief introduction of the asymptotic homogenization method. Then the topology

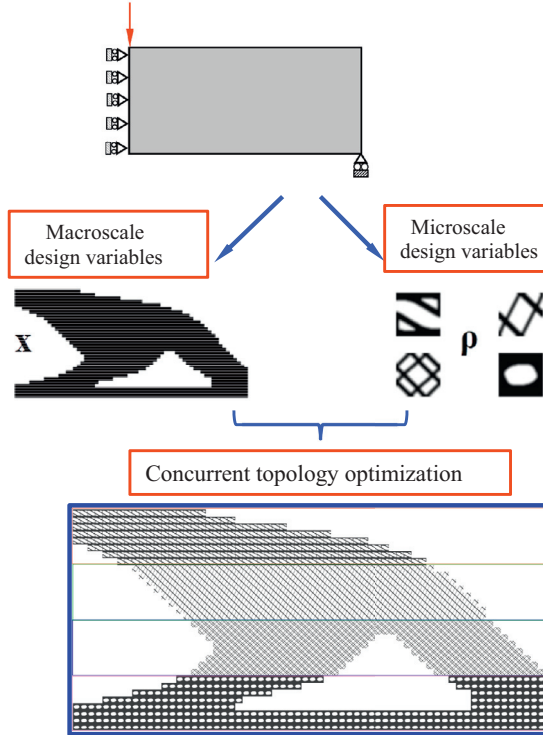


Fig. 1. Illustration of two types of design variables in the concurrent design model.

optimization framework and sensitivity analysis with respect to the macroscale and microscale design variables are presented. In Section 4, we first show validation of the average porosity constraint, and several numerical examples regarding single-material and bi-material lattice structures are given. We also verify an optimized graded lattice structure through finite element simulations, and compare its predicted load-bearing capacity with those of the designs with solid material and uniform lattice microstructures.

2. Concurrent design model of layer-wise graded lattice structures

2.1. Design variables for two-scale concurrent design

In our considered two-scale concurrent design problem, two types of design variables \mathbf{x} and ρ are introduced, which respectively represent material distributions in the macroscale and microscale structures. As shown in Fig. 1, the macroscale design variables \mathbf{x} indicate the presence/absence of material in the macroscale elements, which are to be driven to either 0 or 1 in the optimization process. The microstructural design variables ρ define all the microstructural topologies. Note that all design variables in the two scales are to be optimized simultaneously. Using this concurrent model, we aim to obtain well-defined designs of two-scale layer-wise graded structures (each layer consists of one type of unit cells).

2.2. Structural coverage constraint and average porosity constraint

In order to achieve a two-scale layer-wise structural design as shown in Fig. 2, we now define a structural coverage constraint and an average porosity constraint respectively as

$$G_{SCC} = \sum_{l=1}^L \sum_{k=1}^m x_{k,l} A_{k,l} - f_1 |\Omega| \quad (1)$$

$$G_{APC} = \sum_{l=1}^L \sum_{k=1}^m x_{k,l} A_{k,l} \left(\left(\sum_{e=1}^M \rho_{l,e} S_{l,e} \right) / |\mathbf{Y}_l| \right) - (1 - f_2) \sum_{l=1}^L \sum_{k=1}^m x_{k,l} A_{k,l} \quad (2)$$

Here, the structural coverage constraint and the average porosity constraint restrict the area (volume in 3D cases) coverage of different microstructural materials in the macroscale and the average porosity ratio of the two-scale structure,

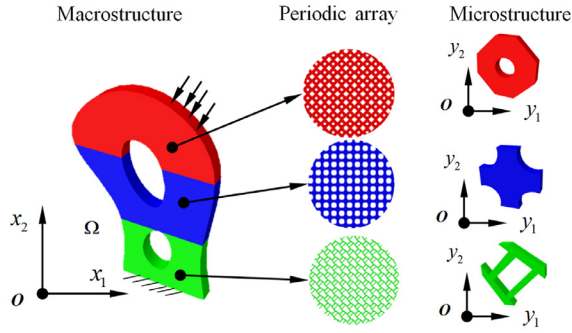


Fig. 2. A macrostructure and its layer-wise graded microstructures. The Cartesian coordinate systems (x_1, x_2) and (y_1, y_2) refer to the macroscale and microscale design spaces.

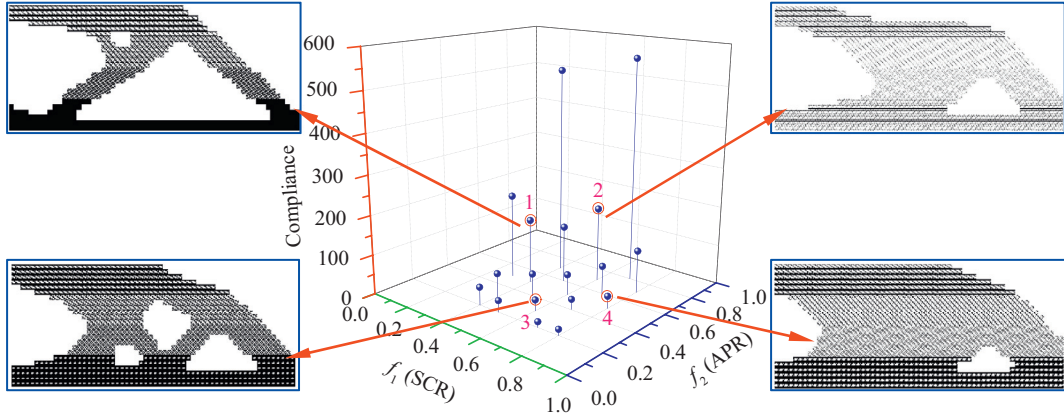


Fig. 3. Schematic illustration of influence of the structural coverage ratio f_1 (SCR) and average porosity ratio f_2 (APR) on the structural compliance.

respectively; $x_{k,l}$ is the macroscale design variable of the k th macroscale element at the l th layer; $\rho_{l,e}$ is the microscale design variable of the e th element at the l th layer, f_1 is the specified structural coverage ratio, and f_2 is the target average porosity ratio of all the microstructures; L is the total number of layers; $|\Omega|$ is the volume of the macroscale design domain and $|\mathbf{Y}_l|$ is the volume of the unit cell in the l th layer; m and M denote the total numbers of macroscale elements located in each layer and the microscale elements of each unit cell, respectively. The symbol $A_{k,l}$ represents the volume of the k th macroscale element at the l th layer, and $S_{l,e}$ is the e th microscale element volume of unit cell in the l th layer. It is noted that the actual material usage is $f_1(1 - f_2)|\Omega|$. In Fig. 3, some illustrative design samples are given in the interval $[0, 1]$ of f_1 and f_2 to show their impacts on the structural stiffness.

3. Formulation of topology optimization and sensitivity analysis

3.1. Asymptotic homogenization of unit cells

In the considered design model of layer-wise graded lattice structures, the size of all microstructures are considered to be much smaller than the layer thickness. Therefore, asymptotic homogenization method (AHM) (Hassani & Hinton, 1998) can be used to compute the effective elastic properties of the microstructural materials. Here, only the first-order terms in the asymptotic expansion are considered in the homogenization method and the effective elasticity tensor \bar{D}_{ijpq} of a unit cell can be computed by

$$\bar{D}_{ijpq} = \frac{1}{|\mathbf{Y}|} \int_{\mathbf{Y}} \left(D_{ijpq}(\mathbf{y}) - D_{ijkt}(\mathbf{y}) \frac{\partial \chi_k^{pq}}{\partial y_t} \right) d\mathbf{y} \quad i, j, p, q = 1, 2, \dots, d \quad (3)$$

or in an equivalent mutual energy form (Sigmund, 1994; Thomsen, Wang, & Sigmund, 2018)

$$\bar{D}_{ijpq} = \frac{1}{|\mathbf{Y}|} \int_{\mathbf{Y}} D_{rskt} (\varepsilon_{rs}^{0(ij)} - \varepsilon_{rs}^*(\chi^{ij})) (\varepsilon_{kt}^{0(pq)} - \varepsilon_{kt}^*(\chi^{pq})) d\mathbf{y} \quad i, j, p, q = 1, 2, \dots, d \quad (4)$$

where D_{rskt} is the elasticity tensor of the constituent material, d is the spatial dimension ($d = 2$ for the considered two-dimensional problems), \mathbf{Y} and $|\mathbf{Y}|$ are respectively the domain and volume of the periodic unit cell. The elasticity tensor

has the form $D_{rskt} = ED_{rskt}^0$, in which D_{rskt}^0 and E are respectively the dimensionless isotropic elasticity tensor and Young's modulus of the base material.

In Eqs. (3) and (4), the characteristic displacement field χ of the unit cell is the solution to the following microscale problem

$$\int_Y D_{rskt} \varepsilon_{rs}^*(\chi^{ij}) \varepsilon_{kt}(\delta^{pq}) dy = \int_Y D_{rskt} \varepsilon_{rs}^0(\chi^{ij}) \varepsilon_{kt}(\delta^{pq}) dy \quad \forall \delta \in \mathbf{U}_{\text{mic}} \quad (5)$$

where δ^{pq} is the virtual displacement, and $\mathbf{U}_{\text{mic}} = \{\delta : \delta \text{ is } |Y| - \text{periodic}\}$ is the virtual displacement space of the unit cell. The fluctuation strain $\varepsilon_{rs}^*(\chi^{ij})$ is defined by the strain-displacement relation $\varepsilon_{rs}^*(\chi^{ij}) = (\partial \chi_r^{ij}/\partial y_s + \partial \chi_s^{ij}/\partial y_r)/2$, and $\varepsilon_{rs}^{0(ij)}$ represents the three independent unit test strain fields, namely the horizontal unit strain $\varepsilon_{rs}^{0(11)} = (1, 0, 0)^T$, the vertical unit strain $\varepsilon_{rs}^{0(22)} = (0, 1, 0)^T$ and the unit shear strain $\varepsilon_{rs}^{0(12)} = (0, 0, 1)^T$.

3.2. Mathematical statement of topology optimization

The optimization formulation is expressed as

$$\begin{aligned} \min_{\mathbf{x}, \rho} : J(\mathbf{x}, \rho) &= \mathbf{f}^T \mathbf{u} \\ \text{s.t.} : a(\mathbf{u}, \mathbf{v}) &= l(\mathbf{v}) \quad \forall \mathbf{v} \in \mathbf{U}_{\text{mac}} \\ \int_{Y_l} D_{rskt} \varepsilon_{rs}^{*(ij)} \varepsilon_{kt}(\delta_l^{pq}) dy &= \int_{Y_l} D_{rskt} \varepsilon_{rs}^{0(ij)} \varepsilon_{kt}(\delta_l^{pq}) dy \quad \forall \delta_l^{pq} \in \mathbf{U}_{\text{mic}}^l, l = 1, 2, \dots, L \\ G_{\text{SCC}} &\leq 0 \quad (\text{SCC}) \\ G_{\text{APC}} &\leq 0 \quad (\text{APC}) \\ 0 \leq x_i &\leq 1, i = 1, 2, \dots, N \\ 0 < \rho_{\min} &\leq \rho_{l,e} \leq 1, e = 1, 2, \dots, M \end{aligned} \quad (6)$$

where the objective function J is the macrostructural compliance; $\mathbf{x} = \{x_1, x_2, \dots, x_N\}^T$ and $\rho = \{\rho_1^T, \rho_2^T, \dots, \rho_L^T\}^T$ are respectively the design variable vectors for the macrostructure and microstructures, where $\rho_l = \{\rho_{l,1}, \rho_{l,2}, \dots, \rho_{l,M}\}^T$ ($l = 1, 2, \dots, L$) collects the microscale design variables in the l th layer, and L is the number of total layers in the pre-scribed direction. Here, N denotes the total number of macroscale design variables, and each microstructure has M design variables. The lower bound of microscale design variables ρ_{\min} is set to be a small value to avoid numerical singularity. The symbols \mathbf{u} and \mathbf{v} are the displacements and virtual displacements of the macrostructure, \mathbf{f} is nodal load vector, and \mathbf{U}_{mac} is the virtual displacement space of the macrostructure. The energy bilinear form and load linear form are respectively

$$a(\mathbf{u}, \mathbf{v}) = \sum_{l=1}^L \int_{\Omega_l} \boldsymbol{\varepsilon}(\mathbf{u}) : \tilde{\mathbf{D}}_l : \boldsymbol{\varepsilon}(\mathbf{v}) d\Omega \quad (7)$$

$$l(\mathbf{v}) = \int_{\Omega} \mathbf{p} \cdot \mathbf{v} d\Omega + \int_{\Gamma_t} \mathbf{t} \cdot \mathbf{v} d\Gamma \quad (8)$$

where \mathbf{p} is the mechanical body force and \mathbf{t} is the surface traction applied on the boundary Γ_t .

In the macroscale design problem, the material elasticity tensor for the k th element of the l th layer is interpolated as $\tilde{\mathbf{D}}_{k,l} = \mathbf{D}_{\min} + x_{k,l}^\eta (\bar{\mathbf{D}}_{k,l} - \mathbf{D}_{\min})$. Here, $\bar{\mathbf{D}}$ is the effective elasticity tensor of the corresponding microstructured material, and it is to be determined by the asymptotic homogenization method in Eq. (4). In this study, we set the macroscale penalty factor to be $\eta = 4$, and choose $\mathbf{D}_{\min} = 10^{-6} \mathbf{D}_0$ to avoid numerical singularity of the macrostructure analysis.

Using the SIMP model, the Young's modulus E for a microstructure elements is related to the microscale design variables with the power law penalized interpolation model (Bedsoe & Sigmund, 1999). For instance, in the bi-material case, the material interpolation model is expressed as

$$E = \rho^\xi E_H + (1 - \rho^\xi) E_S \quad (9)$$

where E_S and E_H are the Young's moduli of the soft and hard materials, respectively. In this study, the penalty factor is set to be $\xi = 5$.

It is noted that, there is only one average porosity constraint regardless of the total number of microstructures in our proposed model, therefore the complexity of the optimization model remains reasonable.

3.3. Sensitivity analysis

The objective function in Eq. (6) contains the design variables of two scales, and it can be written in the discretized finite element form as

$$J(\mathbf{x}, \boldsymbol{\rho}) = \sum_{l=1}^L \sum_{k=1}^m (\mathbf{u}_{k,l})^T \mathbf{k}_{k,l} \mathbf{u}_{k,l} \quad (10)$$

where $\mathbf{k}_{k,l}$ and $\mathbf{u}_{k,l}$ are the element stiffness matrix and nodal displacement vector of the k th macroscale element in the l th layer. The element stiffness matrix has the following form

$$\mathbf{k}_{k,l} = \int_{\Omega_{k,l}} \mathbf{B}^T \tilde{\mathbf{D}}_{k,l} \mathbf{B} d\Omega \quad (11)$$

where \mathbf{B} is the strain-displacement matrix.

3.3.1. Sensitivity analysis with respect to macroscale design variables

The derivatives of the objective function J with respect to the macroscale design variables defining the material distributions in the structural design domain are

$$\frac{\partial J(\mathbf{x}, \boldsymbol{\rho})}{\partial x_{k,l}} = -(\mathbf{u}_{k,l})^T \frac{\partial \mathbf{k}_{k,l}}{\partial x_{k,l}} \mathbf{u}_{k,l} = -\mathbf{u}_{(k,l)}^T \left[\int_{\Omega_{k,l}} \mathbf{B}^T (\eta x_{k,l}^{\eta-1} (\bar{\mathbf{D}}_{k,l} - \mathbf{D}_{\min})) \mathbf{B} d\Omega \right] \mathbf{u}_{k,l} \quad k = 1, 2, \dots, m; \quad l = 1, 2, \dots, L \quad (12)$$

where $\bar{\mathbf{D}}_{k,l}$ is computed by using the asymptotic homogenization method. Eq. (12) shows that the sensitivities of the objective function with respect to the macroscale design variables are functions of both macroscale and microscale design variables of the corresponding layer.

The derivatives of the structural coverage constraint and the average porosity constraint can be easily obtained as

$$\frac{\partial G_{SCC}}{\partial x_{k,l}} = A_{k,l} \quad k = 1, 2, \dots, m; \quad l = 1, 2, \dots, L \quad (13)$$

$$\frac{\partial G_{APC}}{\partial x_{k,l}} = A_{k,l} \left(\left(\sum_{e=1}^M \rho_{l,e} S_{l,e} \right) / |\mathbf{Y}_l| \right) - (1 - f_2) A_{k,l} \quad k = 1, 2, \dots, m; \quad l = 1, 2, \dots, L \quad (14)$$

3.3.2. Sensitivity analysis with respect to microscale design variables

In this considered layer-wise design model, the microstructure in the l th layer has microscale design variables $\rho_{l,e}$ ($e = 1, 2, \dots, M$). The sensitivity of the objective function with respect to the microscale design variable $\rho_{l,e}$ can be expressed as

$$\begin{aligned} \frac{\partial J(\mathbf{x}, \boldsymbol{\rho})}{\partial \rho_{l,e}} &= -\frac{\partial \sum_{l=1}^L \sum_{k=1}^m (\mathbf{u}_{k,l})^T \mathbf{k}_{k,l} \mathbf{u}_{k,l}}{\partial \rho_{l,e}} \\ &= -\sum_{k=1}^m (\mathbf{u}_{k,l})^T \left[\int_{\Omega_{k,l}} \mathbf{B}^T \left(x_{k,l}^\eta \frac{\partial \bar{\mathbf{D}}_{k,l}}{\partial \rho_{l,e}} \right) \mathbf{B} d\Omega \right] \mathbf{u}_{k,l} \quad l = 1, 2, \dots, L; \quad e = 1, 2, \dots, M \end{aligned} \quad (15)$$

where the first derivate of the effective elastic tensor is

$$\begin{aligned} \frac{\partial \bar{D}_{ijpq}}{\partial \rho_e} &= \frac{1}{|\mathbf{Y}|} \int_{\mathbf{Y}} \frac{\partial D_{rskt}}{\partial \rho_e} \left(\varepsilon_{rs}^{0(ij)} - \varepsilon_{rs}^*(\chi^{ij}) \right) \left(\varepsilon_{kt}^{0(pq)} - \varepsilon_{kt}^*(\chi^{pq}) \right) d\mathbf{y} \\ &= \frac{1}{|\mathbf{Y}|} \int_{\mathbf{Y}} \xi \rho_e^{(\xi-1)} (E_H - E_S) D_{rskt}^0 \left(\varepsilon_{rs}^{0(ij)} - \varepsilon_{rs}^*(\chi^{ij}) \right) \left(\varepsilon_{kt}^{0(pq)} - \varepsilon_{kt}^*(\chi^{pq}) \right) d\mathbf{y} \quad e = 1, 2, \dots, M \end{aligned} \quad (16)$$

The sensitivities of the average porosity constraint G_{APC} with respect to the microscale design variables are

$$\frac{\partial G_{APC}}{\partial \rho_{l,e}} = \sum_{k=1}^m x_{k,l} A_{k,l} \left(S_{l,e} / |\mathbf{Y}_l| \right) - (1 - f_2) \sum_{k=1}^m x_{k,l} A_{k,l} \quad l = 1, 2, \dots, L; e = 1, 2, \dots, M \quad (17)$$

which turn out to be functions of the macroscale design variables. The density filtering method (Andreassen, Clausen, Schevenels, Lazarov, & Sigmund, 2011; Bourdin, 2001; Lazarov & Sigmund, 2011) is adopted to avoid mesh-dependency and checkerboard patterns of the optimization results in both scales.

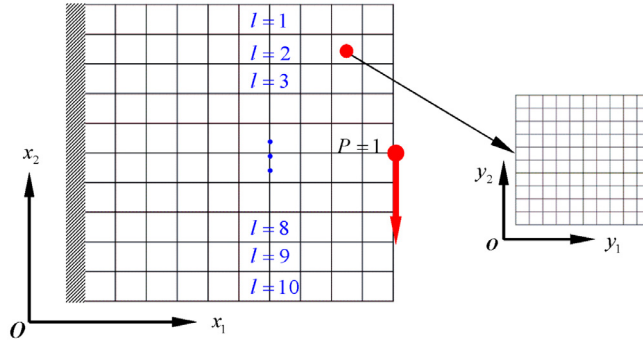


Fig. 4. Finite element discretization (with 10×10 planar square bilinear elements) of the macrostructure and microstructural unit cells used in the sensitivity verification (I denotes the layer number).

Table 1

Solution procedures of concurrent design of layer-wise graded lattice and macrostructures.

Algorithm

- 1: Initialize \mathbf{x}_0 and ρ_0 , and define the boundary conditions and external loads;
- 2: **while** $\max_{k,e,l}(|\mathbf{x}_{k,l}^{i+1} - \mathbf{x}_{k,l}^i|/\mathbf{x}_{k,l}^i, |\rho_{l,e}^{i+1} - \rho_{l,e}^i|/\rho_{l,e}^i) > 10^{-5}$ and Iteration ≤ 300 **do**
- 3: impose PBC on the unit cells;
- 4: compute effective elastic tensors $\bar{\mathbf{D}}$;
- 5: assemble the macro stiffness matrix using results in Step 4;
- 6: compute the objective function $J(\mathbf{x}, \rho)$, the structural coverage constraint G_{SCC} and the average porosity constraint G_{APC} ;
- 7: evaluate sensitivities with respect to macroscale design variables $\partial J/\partial \mathbf{x}_{k,l}$, $\partial G_{SCC}/\partial \mathbf{x}_{k,l}$ and $\partial G_{APC}/\partial \mathbf{x}_{k,l}$, and microscale design variables $\partial J/\partial \rho_{l,e}$, $\partial G_{SCC}/\partial \rho_{l,e}$ and $\partial G_{APC}/\partial \rho_{l,e}$;
- 8: update macroscale design variables \mathbf{x} and microscale design variables ρ using MMA;
- 9: **end while**
- 10: **return** final solutions \mathbf{x} and ρ .

3.3.3. Verification of sensitivity analysis

To verify the sensitivity analysis of the objective function (structural mean compliance), we now consider a ten-layer structure shown in Fig. 4. Both the macrostructure and the ten microstructural unit cells are discretized with 10×10 planar square bilinear elements.

The sensitivities of the objective function with respect to the macroscale and microscale design variables, computed with the mentioned adjoint sensitivity analysis method, are given in Fig. 5. Due to symmetry of the loading and boundary conditions of the macrostructure, only the sensitivities with respect to the microscale design variables of the first 5 layers of microstructures are computed. For comparison, the derivatives of the objective function are also approximated with the finite difference method (FDM), in which the perturbations for all design variables are 0.01%. As can be seen from Fig. 5, the sensitivity results obtained by the two methods agree well with each other.

3.4. Solution procedures

The procedures of the topology optimization are summarized in Table 1. First, we set the initial values of all design variables. Then the homogenization method is used to compute the effective elasticity matrices of the microstructures. After that, adjoint sensitivity analysis is performed as described in Section 3.3. The method of moving asymptotes (MMA, Svanberg, 1987) is then used to update all design variables in this two-scale problem. These procedures are repeated until the prescribed stopping criterion is satisfied.

4. Numerical examples

Several numerical examples regarding concurrent topology optimization of layer-wise graded lattice structures are presented in this section to illustrate the validity of the proposed method. In all examples, the microstructures are discretized into 40×40 uniformly-sized planar square bilinear elements. The initial density distribution of the microstructures is shown in Fig. 6, in which the density values in the black region are 1, and those in the grey region are randomly selected within the interval [0.5, 0.7]. The macroscale design domains are supposed to have ten layers in the specified direction. Connectivity conditions between adjacent microstructure layers are not considered for simplicity. The radii of the artificial density filters (Andreassen et al., 2011; Bourdin, 2001; Lazarov & Sigmund, 2011) are three times of the element sizes in the macroscale and microscale design domains. All the computations were performed on a HP Z840 workstation with two Intel Xeon E5-2687w v3 CPUs (3.10GHz) and 64GB RAM.

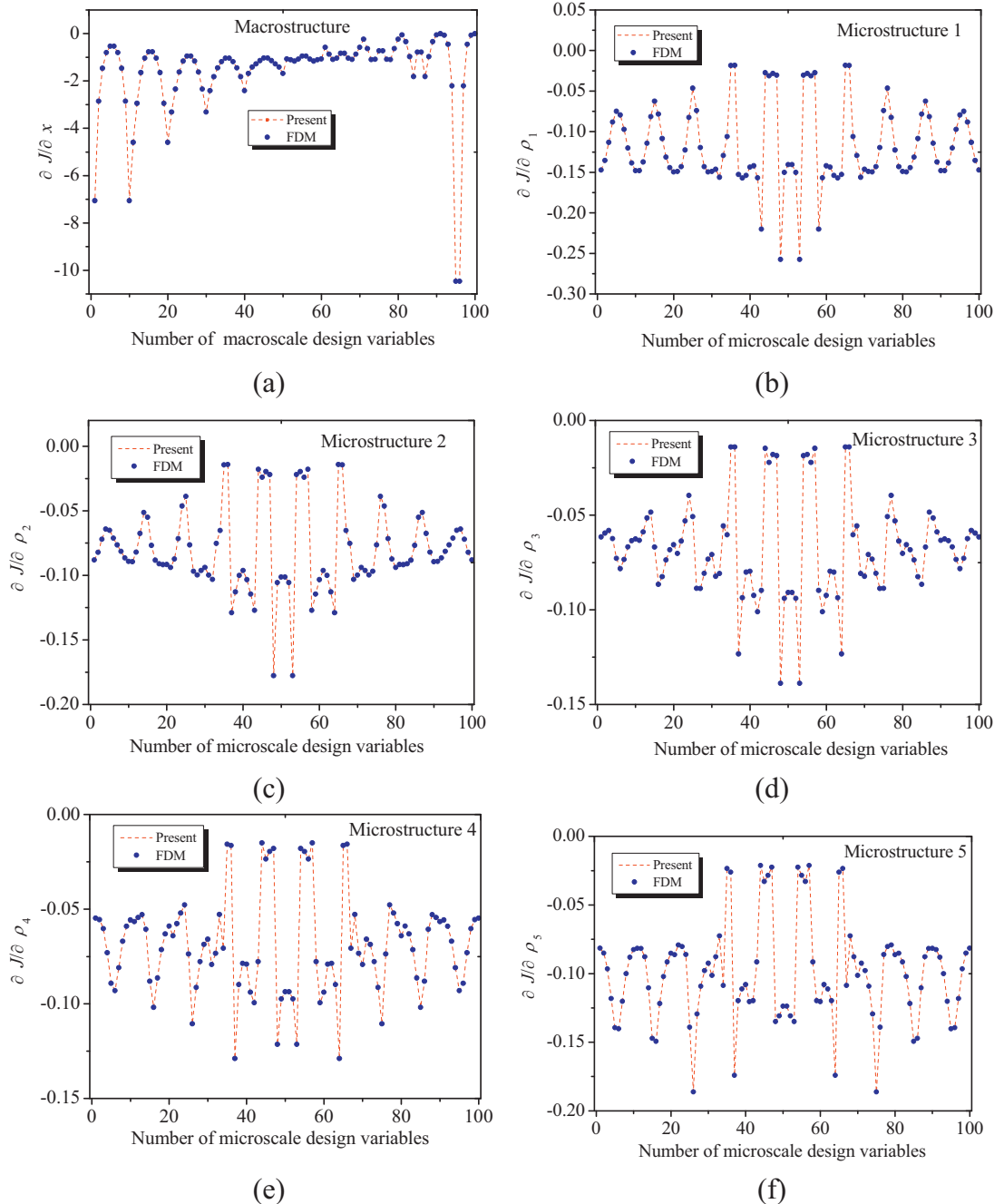


Fig. 5. Comparison of sensitivity results obtained with the present adjoint sensitivity analysis method and the finite difference method (FDM). (a) Sensitivities with respect to macroscale design variables x ; (b)-(f) Sensitivities with respect to microscale design variables ($\rho_i, i = 1, 2, \dots, 5$ for microstructures 1 to 5).

4.1. Effectiveness of average porosity constraint

The layer-wise microstructural design of a cantilever beam is considered to show effectiveness of the average porosity constraint. The macroscale design domain is shown in Fig. 7, and the structure has ten layers in the vertical direction. The Young's modulus of the material is $E = 10$ and the Poisson's ratio is $\nu = 0.3$. The structural coverage ratio is specified to be $f_1 = 1$ (i.e. no voids are allowed in the macrostructure) and the average porosity ratio is $f_2 = 0.5$. The structure is discretized into 60×30 planar square bilinear elements, and the initial values of macroscale design variables are all set to 1.

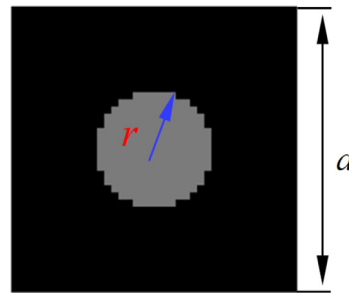


Fig. 6. Initial density distribution for microscale design domain (radius of circular region $r = a/6$).

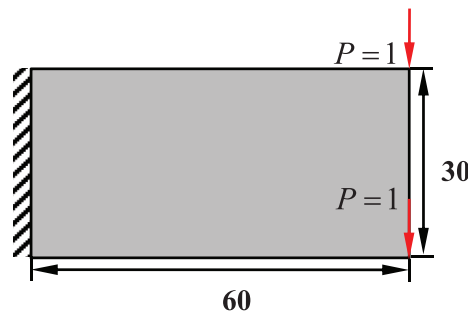


Fig. 7. Design domain of a cantilever beam to show effectiveness of the average porosity constraint.

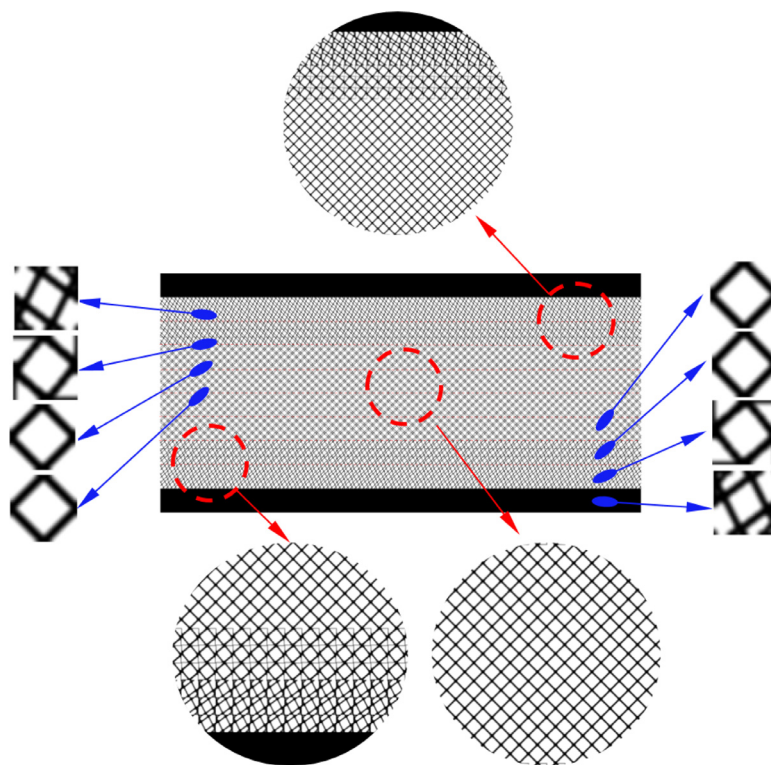


Fig. 8. Optimized microstructures in different layers obtained with a single constraint of average porosity $f_2 = 0.5$.

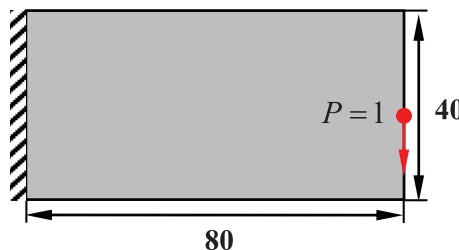


Fig. 9. Design domain for concurrent design of a cantilever beam.

The optimized design, which has a final objective function value $J = 45.93$, is shown in Fig. 8. As shown in the zoomed regions, clear and symmetric layouts of microstructures are obtained. In particular, the upper and lower layers of the structure consist of fully solid unit cells. It is noted that, the obtained microstructures are controlled by the only one average porosity constraint in this design problem, and the proposed design formulation enables the optimizer to improve the overall structural stiffness by changing the topologies and porosities of the unit cells in different layers under the same material usage specified by this constraint.

4.2. Concurrent design of a cantilever lattice beam

We now consider concurrent topology optimization of a layer-wise graded lattice cantilever beam as shown in Fig. 9. The material properties are the same as mentioned in Section 4.1. The design domain is discretized with 80×40 uniformly sized planar square bilinear elements. The structural coverage ratio and the average porosity ratio are set as $f_1 = 0.7$ and $f_2 = 0.4$, respectively. All the elemental densities are set to be 0.7 in the initial macrostructural design.

Starting from the initial microstructures shown in Fig. 6, convergence was achieved after 289 iterations, yielding an objective function compliance value of $J = 13.01$. The optimized designs of the macrostructure and the microstructures are shown in Fig. 10. In Fig. 10(a), a threshold density value of 0.5 is used to show a clear black-and-white distribution of materials. As can be seen, the macroscale topology is symmetric with respect to the central axis of the design domain. All the optimized microstructures, with their effective elasticity matrices, are also given in Fig. 10(b). It is found that the optimized layouts of the microstructures are also symmetric about the central axis of the macrostructure.

The iteration histories given in Fig. 11 indicate a steady iteration. Moreover, both the structural coverage ratio and the average porosity ratio reached their prescribed values in the final design. The microstructural volume fractions, as shown in Fig. 11(b) and (c), converged to the final values 1.000, 0.478, 0.483, 0.509, 0.558, 0.558, 0.509, 0.483, 0.478 and 1.000.

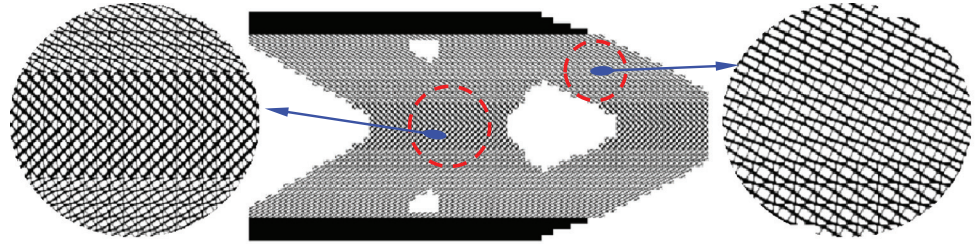
Clearly, the final topologies of the microstructures are controlled by the combined effects of the structural coverage constraint and the average porosity constraint. As can be found from Fig. 10, the microstructures located in the top and bottom regions of the macrostructure contain much more materials than those in other regions. This is because these regions require higher stiffness to resist the structural deformation under the applied force. In most of the optimized microstructures, the material tends to distribute along the principle stress directions of the macrostructure. Though most parts of optimized microstructures are connectable between different layers, as shown in Fig. 10(a), there are still some mismatches. It is worth noting that connectivity of microstructures can be ensured by imposing additional constraints to the unit cell design at the cost of compromising the structural performance, see Wang et al. (2017) and Cheng, Liu, and To (2018).

As two special cases, the optimization solutions for single-scale design and concurrent design with uniform microstructures are also obtained with the proposed method for the purpose of comparison, as given in Fig. 12(a) and (b), respectively. Here, the structural coverage and average porosity ratios are set to be $f_1 = 0.42$, $f_2 = 0$ in the former case and $f_1 = 0.70$, $f_2 = 0.4$ in the latter. This means that the total material mass in both designs are the same as that used by the design shown in Fig. 10. The mean compliances of the two designs are $J = 10.39$ and $J = 20.69$, respectively.

When comparing the objective function values of the three designs shown in Figs. 10 and 12, it is not surprising to find that the two-scale layer-wise graded structure (Fig. 10(a)) exhibits a lower stiffness than the single-scale solid material macrostructure with fully solid material (Fig. 12(a)), but a much higher stiffness than the structure with uniform microstructures (Fig. 12(b)). It should be noted that such a two-scale porous lattice structure is generally more capable of resisting structural buckling (Wu, Aage, Westermann, & Sigmund, 2018).

Some optimized designs for different combinations of the structural coverage ratio and average porosity ratio are listed in Tables 2 and 3. In Table 2, the average porosity ratio is fixed at $f_2 = 0.5$, and the structural coverage ratio is set to be $f_1 = 0.6, 0.7, 0.8$ and 0.9 . It is seen that both the macrostructural and microstructural topologies change with the structural coverage ratio. Also, the structural stiffness increases with that of the structural coverage ratio due to increased usage of total material mass.

In Table 3, the structural coverage ratio is specified as $f_1 = 0.65$, but the average porosity ratio takes different values of $f_2 = 0.3, 0.4, 0.5$ and 0.6 . For an increased average porosity ratio, as the total material usage is decreased, the porosity of the lattice materials on the top and bottom edges becomes larger (see cases (c) and (d)). This is interesting considering the fact



(a)



$$\begin{bmatrix} 10.988 & 3.296 & 0 \\ 3.296 & 10.988 & 0 \\ 0 & 0 & 3.846 \end{bmatrix} \quad \begin{bmatrix} 1.705 & 0.521 & -0.767 \\ 0.521 & 0.480 & -0.124 \\ -0.767 & -0.124 & 0.487 \end{bmatrix} \quad \begin{bmatrix} 1.580 & 0.513 & -0.649 \\ 0.513 & 10.988 & 0.096 \\ -0.649 & -0.096 & 0.447 \end{bmatrix} \quad \begin{bmatrix} 1.854 & 0.556 & -0.635 \\ 0.556 & 0.933 & -0.088 \\ -0.635 & -0.088 & 0.528 \end{bmatrix}$$

1

2

3

4



$$\begin{bmatrix} 1.166 & 1.122 & -0.446 \\ 1.122 & 1.988 & -0.253 \\ -0.446 & -0.253 & 1.055 \end{bmatrix} \quad \begin{bmatrix} 1.166 & 1.122 & -0.446 \\ 1.122 & 1.988 & -0.253 \\ -0.446 & -0.253 & 1.055 \end{bmatrix} \quad \begin{bmatrix} 1.854 & 0.556 & -0.635 \\ 0.556 & 0.933 & -0.088 \\ -0.635 & -0.088 & 0.528 \end{bmatrix} \quad \begin{bmatrix} 1.580 & 0.513 & -0.649 \\ 0.513 & 0.596 & -0.096 \\ -0.649 & -0.096 & 0.447 \end{bmatrix}$$

5

6

7

8



$$\begin{bmatrix} 1.705 & 0.521 & -0.767 \\ 0.521 & 0.480 & -0.124 \\ -0.767 & -0.124 & 0.487 \end{bmatrix}$$

9

$$\begin{bmatrix} 10.988 & 3.296 & 0 \\ 3.296 & 10.988 & 0 \\ 0 & 0 & 3.846 \end{bmatrix}$$

10

(b)

Fig. 10. Optimized topologies for the two-scale layer-wise structure (with structural coverage constraint $f_1 = 0.6$ and average porosity constraint $f_2 = 0.4$).
 (a) Two-scale cantilever structure; (b) Ten microstructures and effective elasticity matrices.

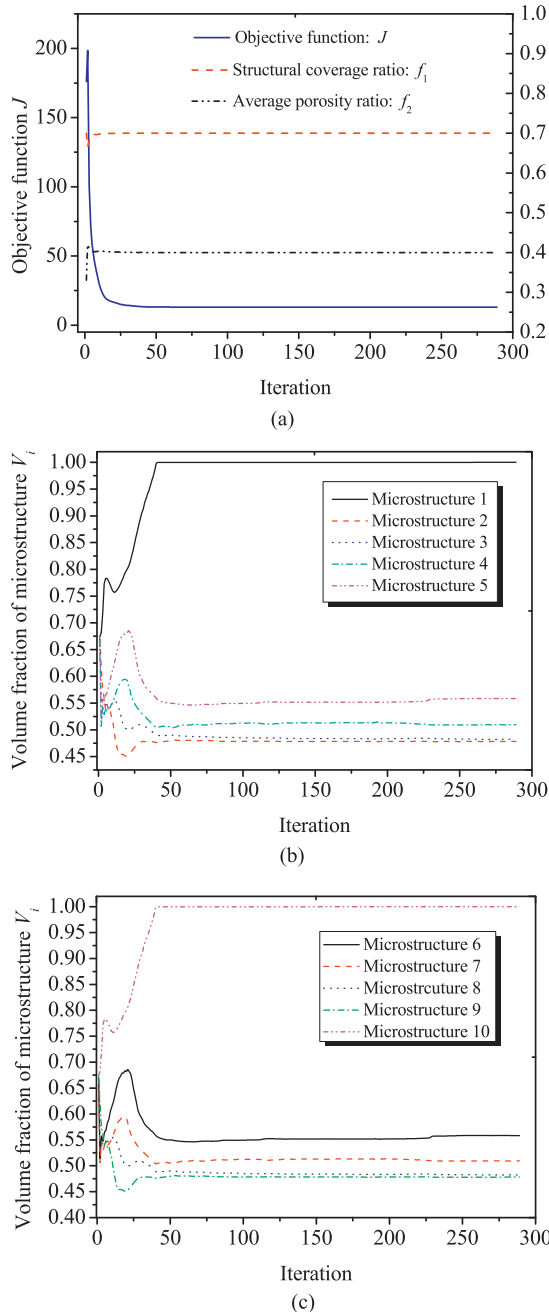


Fig. 11. Iteration histories for the layer-wise cantilever beam design. (a) Objective function J , structural coverage ratio f_1 and average porosity ratio f_2 ; (b) and (c) Volume fractions of the optimized microstructures V_i ($i = 1, 2, \dots, 10$).

that the bar members of a conventional single-scale topology optimized design only become thinner when a lower volume of material is allowed.

4.3. Concurrent design of a curved beam and a circular ring structure

In this example, we use the proposed method to optimize a layer-wise curved beam (shown in Fig. 13) and a circular ring structure (shown in Fig. 14). The outer and inner radii of both structures are $r_{\text{out}} = 25$ and $r_{\text{inner}} = 15$. The Young's modulus and Poisson's ratio of the material are $E_H = 200$ and $\nu = 0.3$, respectively. Both structures have 40 layers of microstructures. They are discretized into 5000 quadrilateral bilinear elements, and the element sizes in each layer are uniform. It should be noted that the microstructure orientations are independent of their positions.

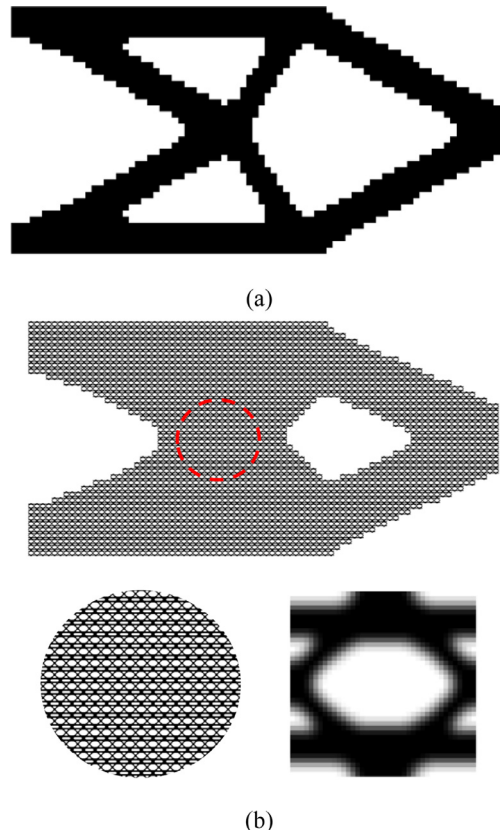


Fig. 12. Two special cases of optimization results. (a) Single-scale design with fully solid material (with structural coverage constraint $f_1 = 0.42$ and average porosity constraint $f_2 = 0$). (b) Two-scale design with uniform microstructure (with structural coverage constraint $f_1 = 0.7$) average porosity constraint $f_2 = 0.4$.

Table 2

Comparison of structural mean compliance for different structural coverage ratio f_1 and fixed average porosity ratio $f_2 = 0.5$.

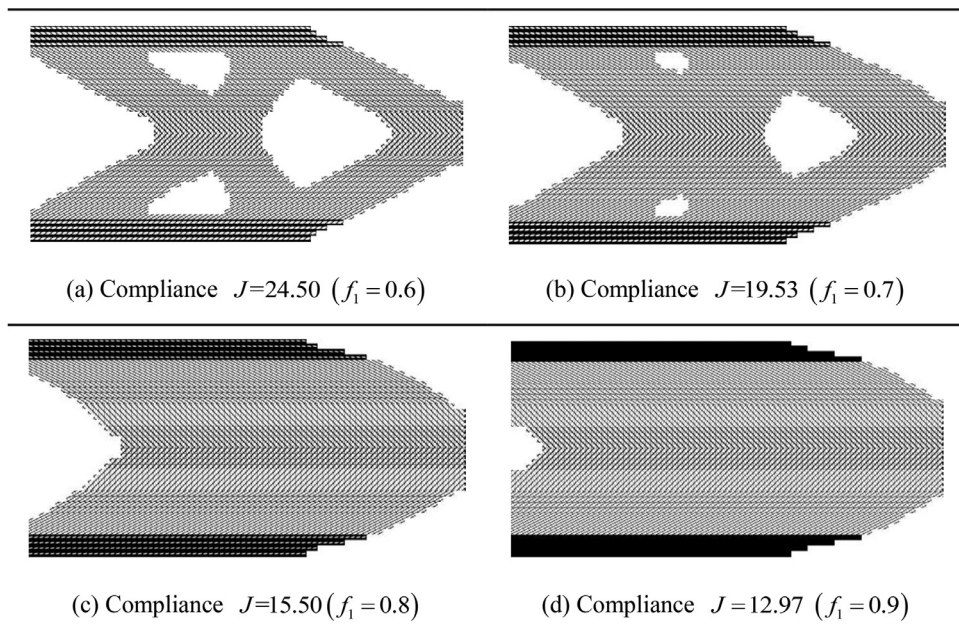


Table 3

Comparison of structural mean compliance for fixed structural coverage ratio $f_1 = 0.65$ and different structural coverage ratio f_2 .

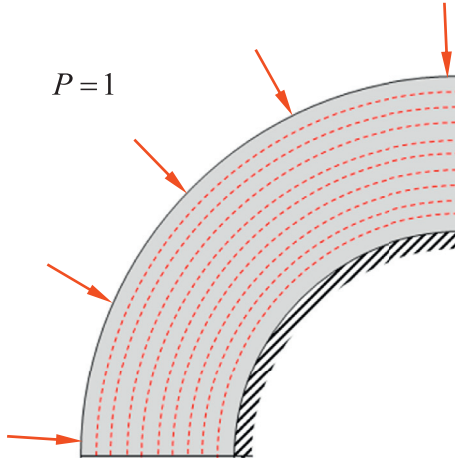
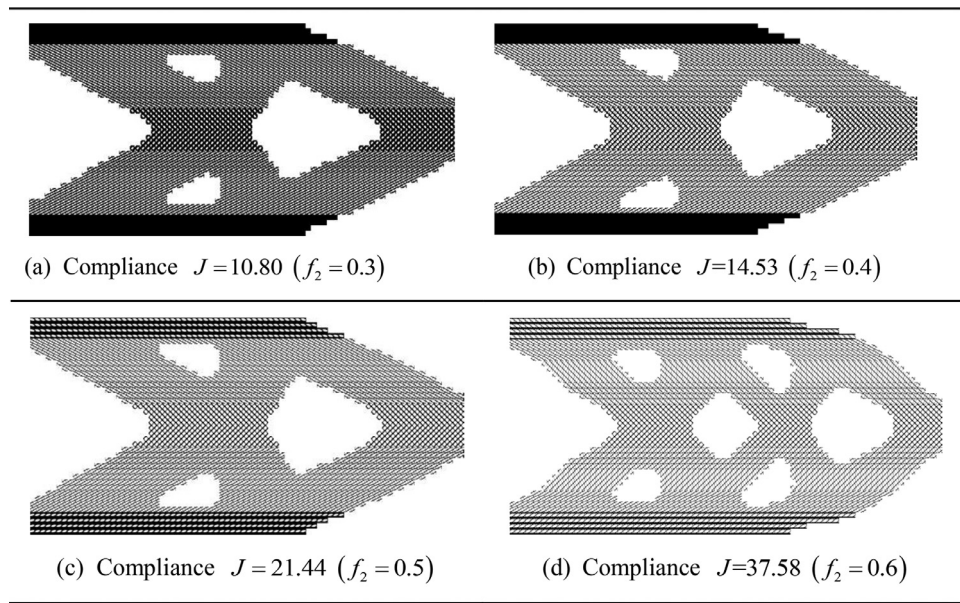


Fig. 13. A curved beam subjected to distributed nodal forces in the radial direction.

For the curved beam design, the structural coverage and average porosity ratios are given as $f_1 = 0.8$ and $f_2 = 0.4$, respectively. The optimized design is shown in Fig. 15, and its objective function compliance value is $J = 15856.60$. It is seen that the inner fixed regions contain only fully solid material.

In the design of the circular ring structure, the constraints are given as $f_1 = 0.6$ and $f_2 = 0.4$. Making use of symmetry, we consider one quarter of the structure as the design domain. The optimized design is given in Fig. 16, which has an objective function compliance value $J = 196.4$. Here, the microstructures of the outer and inner edges become fully solid.

4.4. Concurrent design of a bi-material simply supported beam

We now employ the proposed optimization model in the concurrent design of a simply supported beam with layer-wise microstructures. The design domain of one half of the structure is shown in Fig. 17. Here, the Young's moduli of the hard and soft materials are respectively $E_H = 10$ and $E_S = 1$, and their Poisson's ratios are $\nu = 0.3$. This macrostructure is discretized into 100×40 planar square bilinear elements, and the initial densities of all the macroscale elements are 0.6. We restrict the structural coverage ratio to be $f_1 = 0.6$ and set $f_2 = 0.4$, which means that the ratio between the soft and hard material usage is 0.6667.

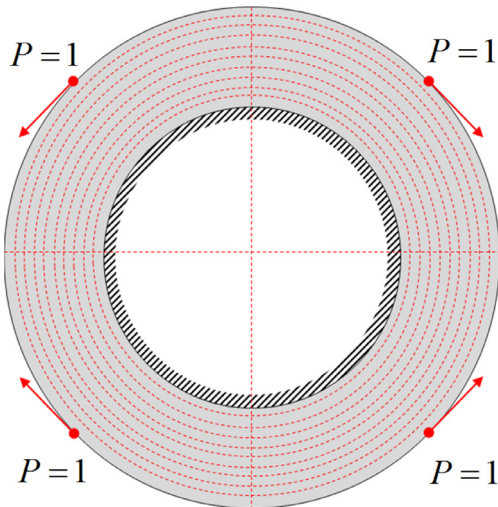


Fig. 14. A circular ring structure subjected to concentrated forces in the circumferential direction.

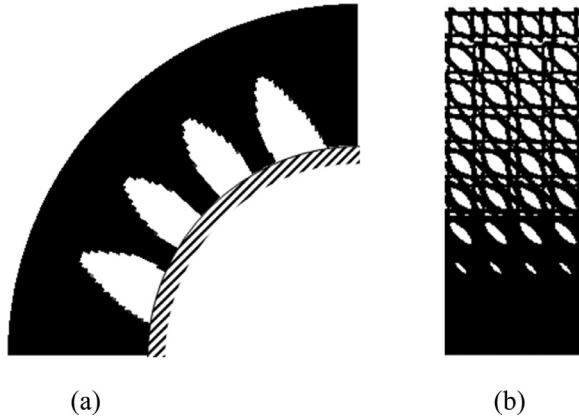


Fig. 15. Optimized design of the curved beam (with structural coverage constraint $f_1 = 0.8$ and average porosity constraint $f_2 = 0.4$). (a) Macrostructure; (b) Microstructures.

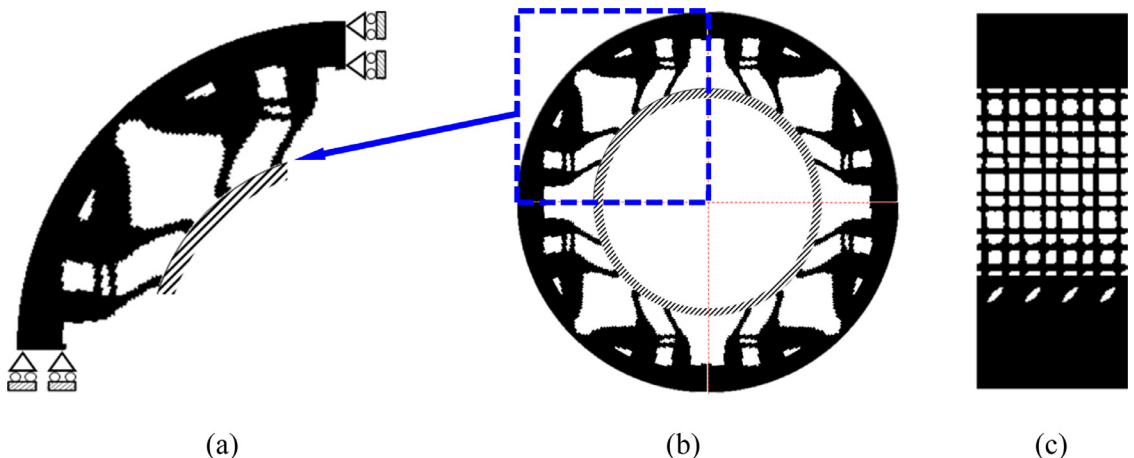


Fig. 16. Optimized design of the circular ring structure (with structural coverage constraint $f_1 = 0.6$ and average porosity constraint $f_2 = 0.4$). (a) One quarter of macrostructure; (b) Whole macrostructure; (c) Microstructures.

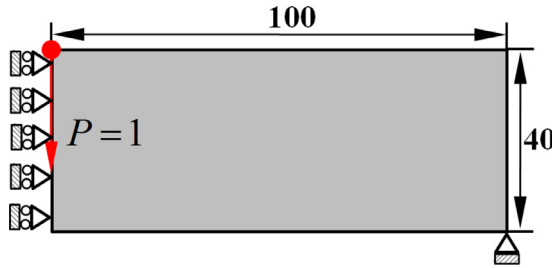
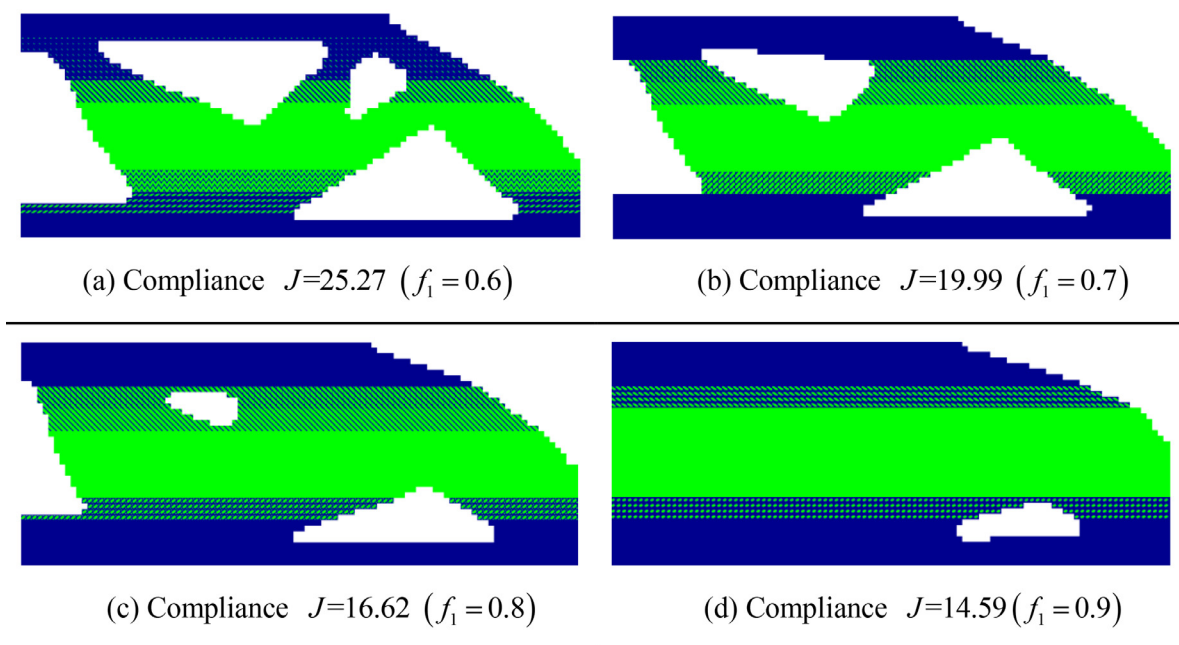


Fig. 17. Design domain of half of the simply supported beam.

Table 4

Comparison of structural mean compliance of bi-material structures for different values of f_1 and fixed value of $f_2 = 0.5$.

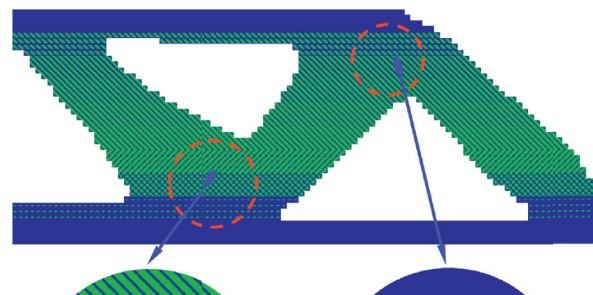


The optimization result has an objective function compliance value of $J = 21.00$. The optimized design and iteration histories are given in Figs. 18 and 19, respectively. In the figures, the blue and green colors represent the hard and soft materials, respectively. In Fig. 18, the microstructures located at the top and bottom boundaries consist of only hard material. Such a configuration is similar to the graded beam design using particle mixing materials (Birman & Byrd, 2007; Jha et al., 2013), while still possessing good manufacturability suitable for advanced multi-material additive manufacture.

For comparison, we also show in Fig. 20 the optimization results of the single-scale solid bi-material structure (compliance $J = 16.51$) and the two-scale structure composed of uniform bi-material microstructures (compliance $J = 28.96$). Both designs have the same usage of hard and soft materials as the one given in Fig. 18.

The single-scale solid bi-material structure shown in Fig. 20(a) has a higher stiffness than the two-scale design with graded microstructures given in Fig. 18. However, it possesses some thin bars, which are prone to instability caused by local buckling under external loads.

We also study the effects of the constraints f_1 and f_2 . In Table 4, the ratio between the soft material volume and the total material volume is fixed at $f_2 = 0.5$, and the structural coverage ratio is set to be $f_1 = 0.6, 0.7, 0.8$ and 0.9 . In Table 5, the structural coverage ratio is fixed at $f_1 = 0.65$, while the ratio between the soft material volume and the total material volume are specified to be $f_2 = 0.3, 0.4, 0.5$ and 0.6 . As can be seen, the top and bottom layers of all the optimized designs consist of only hard material, and the central regions are mainly composed of the soft material.



(a)



$$\begin{bmatrix} 10.988 & 3.296 & 0 \\ 3.296 & 10.988 & 0 \\ 0 & 0 & 3.846 \end{bmatrix} \quad \begin{bmatrix} 3.941 & 1.284 & -0.538 \\ 1.284 & 3.256 & -0.547 \\ -0.538 & -0.547 & 1.415 \end{bmatrix} \quad \begin{bmatrix} 2.319 & 1.118 & -0.606 \\ 1.118 & 2.319 & -0.609 \\ -0.609 & -0.609 & 1.206 \end{bmatrix} \quad \begin{bmatrix} 2.120 & 0.998 & -0.521 \\ 0.920 & 2.120 & -0.521 \\ -0.521 & -0.521 & 1.080 \end{bmatrix}$$

1

2

3

4



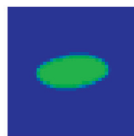
$$\begin{bmatrix} 1.937 & 0.881 & -0.433 \\ 0.881 & 1.937 & -0.433 \\ -0.433 & -0.433 & 0.958 \end{bmatrix} \quad \begin{bmatrix} 1.760 & 0.764 & -0.341 \\ 0.764 & 1.760 & -0.341 \\ -0.341 & -0.342 & 0.837 \end{bmatrix} \quad \begin{bmatrix} 1.683 & 0.685 & 0.248 \\ 0.685 & 1.689 & 0.248 \\ 0.248 & 0.248 & 0.758 \end{bmatrix} \quad \begin{bmatrix} 2.483 & 1.171 & -0.192 \\ 1.171 & 2.504 & -0.189 \\ -0.192 & -0.189 & 1.221 \end{bmatrix}$$

5

6

7

8



$$\begin{bmatrix} 8.770 & 2.256 & 0.084 \\ 2.256 & 7.413 & 0.058 \\ 0.084 & 0.058 & 2.611 \end{bmatrix}$$

9



$$\begin{bmatrix} 10.989 & 3.297 & 0 \\ 3.297 & 10.988 & 0 \\ 0 & 0 & 3.846 \end{bmatrix}$$

10

(b)

Fig. 18. Optimized topologies for the bi-material layer-wise graded beam structure (white, blue and green colors represent respectively the voids, hard and soft materials) (with structural coverage constraint $f_1 = 0.6$ average porosity constraint $f_2 = 0.4$). (a) Two-scale composite structure; (b) Ten microstructures and effective elasticity matrices. (For interpretation of the references to color in this figure legend, the reader is referred to the web version of this article.)

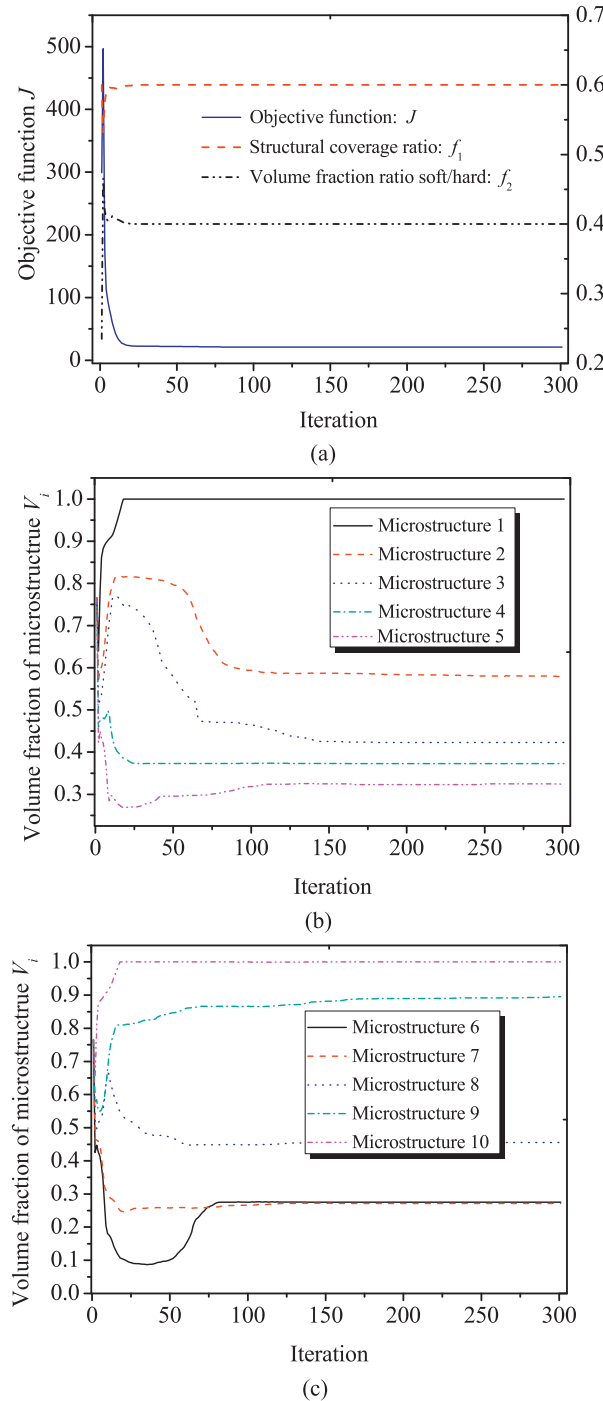


Fig. 19. Iteration histories of bi-material layer-wise graded beam structure. (a) Objective function J , constraint functions f_1 and f_2 ; (b) and (c) Volume fractions of the optimized microstructures V_i ($i = 1, 2, \dots, 10$).

4.5. Comparisons of buckling resistance for optimized MBB beams

In this example, we carry out geometric nonlinear finite element analysis (with self-contact modeling) to compare the post-buckling performance and ultimate load-bearing capacity of optimized MBB (Messerschmitt-Bölkow-Blohm) beams with graded/uniform lattice microstructures (10 layers) and a solid material.

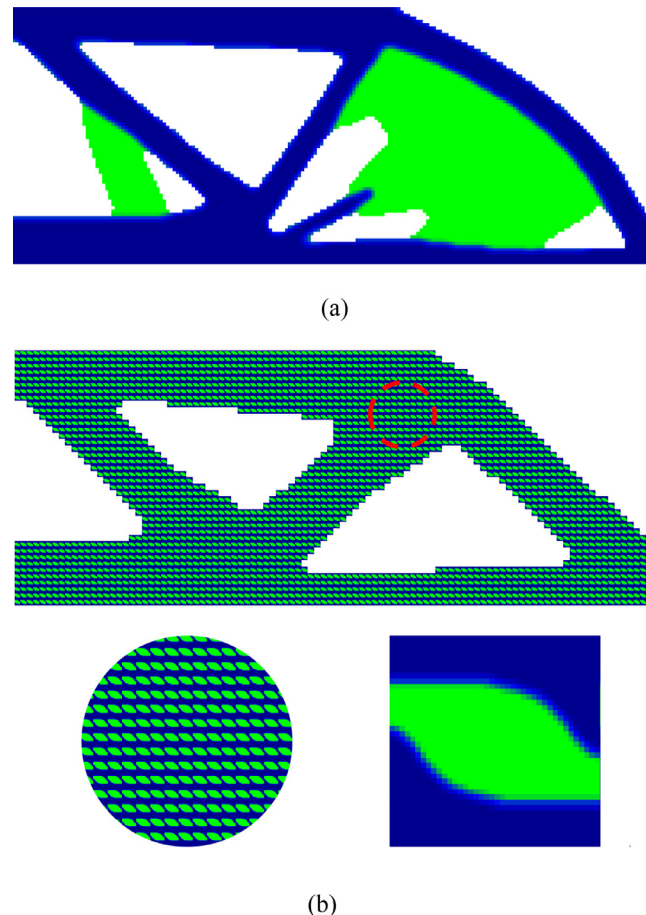
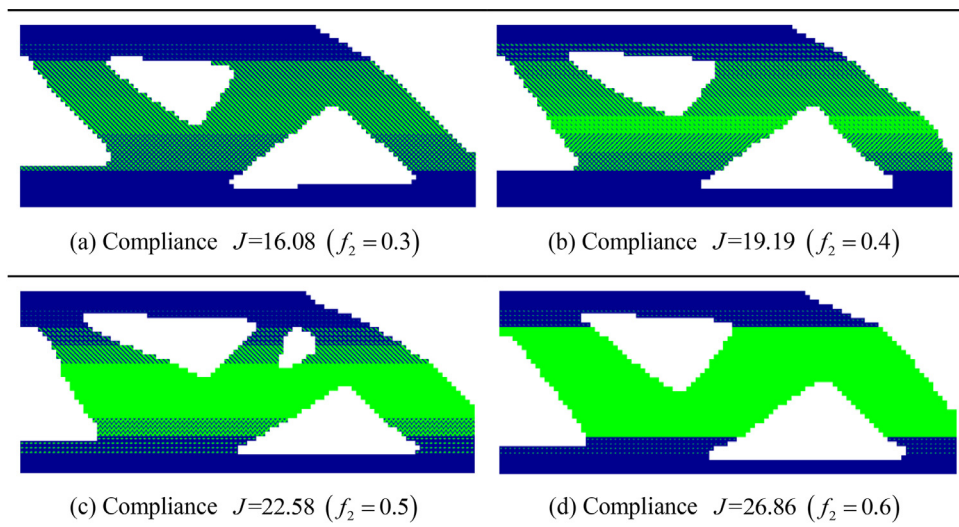


Fig. 20. (a) Optimized single-scale solid bi-material design (with structural coverage constraint $f_1 = 0.36$ and average porosity constraint $f_2 = 0$); (b) Optimized two-scale design with uniform bi-material microstructures (with structural coverage constraint $f_1 = 0.6$ and average porosity constraint $f_2 = 0.4$).

Table 5

Comparison of structural mean compliance for fixed structural coverage ratio $f_1 = 0.65$ and different values of f_2 .



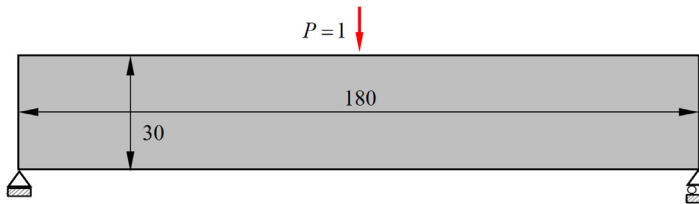


Fig. 21. Design domain of MBB beam.

Table 6

Number of elements in finite element post-buckling analysis of optimized MBB beams.

	Two-scale graded structure	Single-scale solid material structure	Two-scale uniform structure
Bilinear quadrilateral elements (S4R)	41,906	30,046	298,748
Linear triangular elements (S3)	2870	944	32,522

The design domain has a geometric dimension of 180×30 as shown in Fig. 21, and is discretized with 180×30 macroscale planar square bilinear elements. The Young's modulus of the material is $E = 10$ and the Poisson's ratio is $\nu = 0.3$. The optimized designs of the graded lattice structure (compliance $J = 38.94$), the single-scale solid material structure (compliance $J = 31.71$) and the uniform lattice structure (compliance $J = 61.46$) are given in Fig. 22.

The CAD models for such these optimized designs are given in Fig. 23, which share the same material volume fraction ratios of 0.3. The graded and uniform lattice structures are assembled with 3240 microstructures (with size of $1 \times 1 \times 1$ mm). For the graded lattice structure shown in Fig. 22(a), the microstructures of the layers 2–9 have very similar topologies and volume fractions, and thus only one type of representative microstructure is used in our CAD model, as shown in the zoomed region in Fig. 23(a). The material properties of the aluminum alloy with Young's modulus $E = 70$ GPa, Poisson's ratio $\nu = 0.33$ and mass density 2.7×10^3 kg/m³ are considered in the finite element simulations.

We used the explicit dynamic module of the software ABAQUS to simulate the quasi-static compression processes of these structures. The numbers and types of elements we used in the analysis are given in Table 6. In the finite element analysis, the displacement loading rate in the explicit dynamic analysis was set to be 10 m/s, and the out-of-plane deformations were restricted in the analysis. The general contact model was considered, and the tangential behavior friction coefficient was 0.2.

The force-displacement curves, and the deformed shapes for the ultimate strength points obtained by the finite element simulations are plotted in Fig. 24. As expected, the stiffness of the two-scale graded lattice structure is slightly smaller than the solid material structure, but higher than the uniform lattice structure. As the displacement load increase, the two-scale lattice structures (graded and uniform) start to exhibit buckling in some local regions firstly, but the overall structure still possess good load-bearing capacities. Specifically, the reaction force of the two-scale graded lattice structure increases to 3717 N when the applied displacement reaches 11.12 mm. In contrast, the single-scale solid material structure begins to lose its stiffness after buckling, and then reaches the ultimate force of 2283 N for the applied displacement 7.25 mm. The force-displacement curves in Fig. 24 also indicate that the two-scale graded lattice structure can absorb the highest energies than the other two designs. The details of these post-buckling simulations are given in the supplements (animations S1.avi, S2.avi and S3.avi).

These simulations confirm the advantages of the optimized two-scale graded lattice design in comparison with the uniform lattice structure and the single-scale solid material structure.

As mentioned, our finite element analyses were performed with direct modeling of microstructural configurations. It is noted that Clausen et al. reported a previous work on simulation of coated structures with uniform lattice infill, but by using effective material properties of the microstructures (Clausen et al., 2016).

5. Conclusions

We studied concurrent topology optimization of layer-wise lattice structures. New forms of constraints, namely the structural coverage constraint and the average porosity constraint, were introduced into the proposed design model. The topologies of the macrostructure and the microstructures were simultaneously optimized to maximize the overall structural stiffness. This optimization model does not rely on interpreting intermediate densities of macroscale elements as certain porous microstructures, and thus provides a clearer description of the structural topology. This model also enlarges the design space

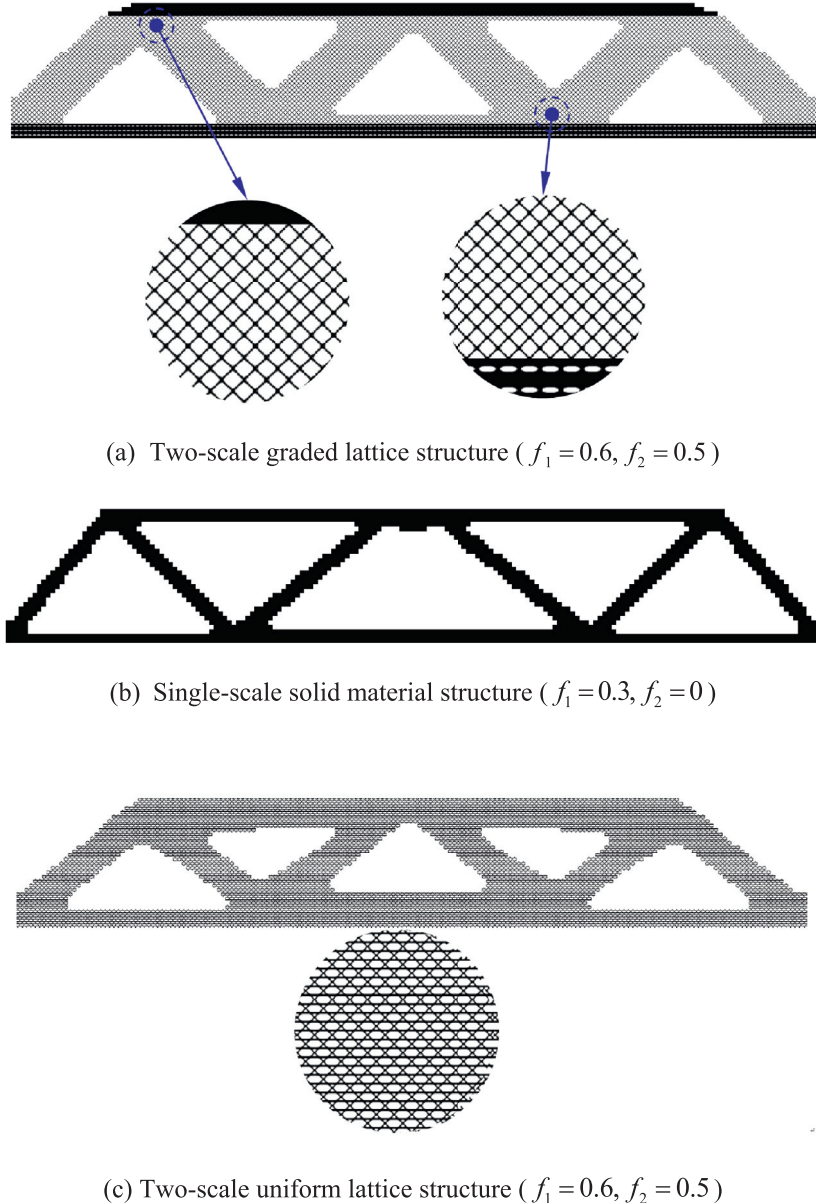


Fig. 22. Optimized designs of an MBB beam. (a) Two-scale graded lattice structure; (b) Single-scale solid material structure; (c) Two-scale uniform lattice structure.

as it integrates the macroscale and microscale design problems. We also extended this model to the design of bi-material graded lattice structures. Numerical examples showed that meaningful topological designs of layer-wise graded lattice structures could be found, and such designs have higher stiffness in comparison to those with uniform lattice microstructures. The influences of the structural coverage ratio and average porosity ratio on the optimized structural design were also studied. Nonlinear finite element post-buckling analysis showed that a two-scale graded lattice structure may have significantly higher ultimate load-bearing and energy absorption capacity than the solid-material and the uniform lattice counterparts under the same material usage.

Though this study concerns only structural stiffness properties, the proposed optimization model provides a basis for the design optimization of hierarchical structures with graded microstructures regarding multi-physic performance or special functionalities such as thermal management, structural vibrations, energy absorption and wave propagation.

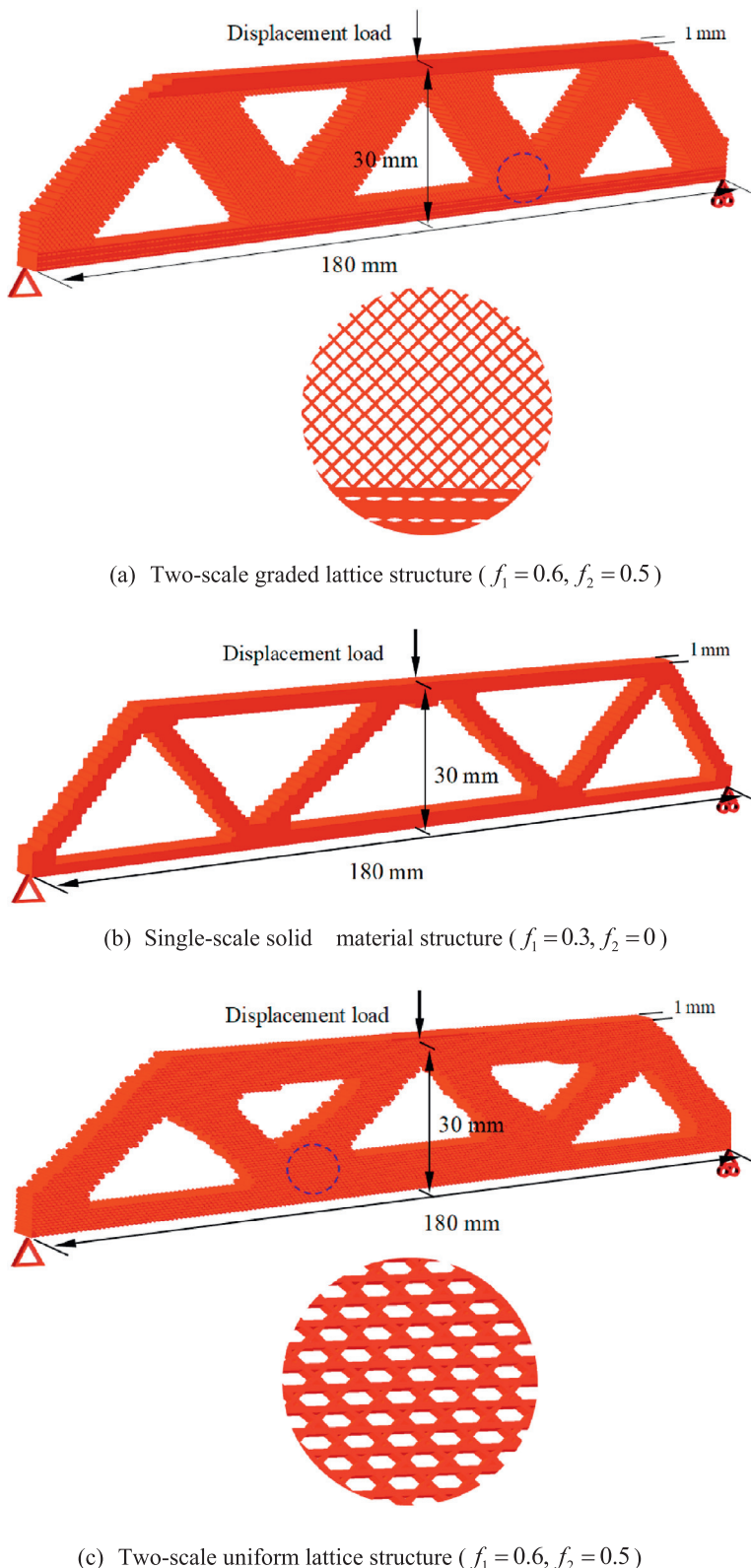


Fig. 23. CAD models of optimized MBB beams with volume fraction 0.3. (a) Two-scale graded lattice structure; (b) Single-scale solid material structure; (c) two-scale uniform lattice structure.

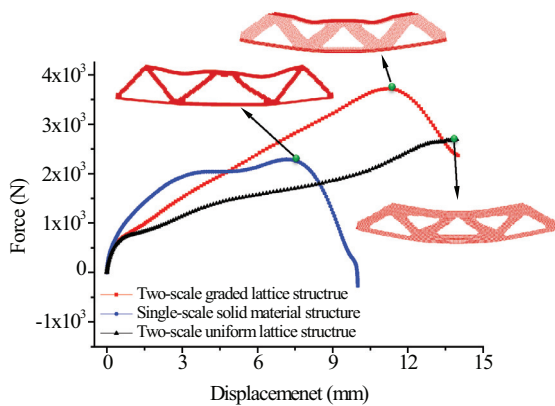


Fig. 24. Force-displacement curves obtained by finite element simulations.

Acknowledgements

Financial support of the National Science Fund for Distinguished Young Scholars (Grant No. 11425207) and the Key Program of National Science Foundation of China (Grant No. U1508209) is gratefully acknowledged. Special thank goes to Dr. Yiqiang Wang from Denmark Technical University for the helpful discussions. We are also grateful to professor Krister Svanberg from Kungliga Tekniska Högskolan for providing the optimization package MMA.

Supplementary material

Supplementary material associated with this article can be found, in the online version, at doi:[10.1016/j.ijengsci.2019.01.006](https://doi.org/10.1016/j.ijengsci.2019.01.006).

References

- Aage, N., Andreassen, E., Lazarov, B. S., & Sigmund, O. (2017). Giga-voxel computational morphogenesis for structural design. *Nature*, 550(7674), 84.
- Andreassen, E., Clausen, A., Schevenels, M., Lazarov, B. S., & Sigmund, O. (2011). Efficient topology optimization in MATLAB using 88 lines of code. *Structural and Multidisciplinary Optimization*, 43(1), 1–16.
- Al-Saeedi, D. S., Masood, S. H., Faizan-Ur-Rab, M., Alomarah, A., & Ponnusamy, P. (2018). Mechanical properties and energy absorption capability of functionally graded F2BCC lattice fabricated by SLM. *Materials & Design*, 144, 32–44.
- Attia, M. A. (2017). On the mechanics of functionally graded nanobeams with the account of surface elasticity. *International Journal of Engineering Science*, 115, 73–101.
- Bendsoe, M. P., & Sigmund, O. (1999). Material interpolation schemes in topology optimization. *Archive of Applied Mechanics*, 69(9–10), 635–654.
- Bendsoe, M. P., & Sigmund, O. (2003). *Topology optimization: Theory, methods, and applications*. Springer.
- Birman, V., & Byrd, L. W. (2007). Modeling and analysis of functionally graded materials and structures. *Applied Mechanics Reviews*, 60, 195–216.
- Bourdin, B. (2001). Filters in topology optimization. *International Journal for Numerical Methods in Engineering*, 50(9), 2143–2158.
- Callewaert, F., Velev, V., Kumar, P., Sahakian, A. V., & Aydin, K. (2018). Inverse-designed broadband all-dielectric electromagnetic metadevices. *Scientific Reports*, 8(1), 1358.
- Cheng, L., Liu, J. K., & To, A. C. (2018). Concurrent lattice infill with feature evolution optimization for additive manufactured heat conduction design. *Structural and Multidisciplinary Optimization*, 1–25.
- Clausen, A., Aage, N., & Sigmund, O. (2016). Exploiting additive manufacturing infill in topology optimization for improved buckling load. *Engineering*, 2, 250–257.
- Coelho, P. G., Fernandes, P. R., Guedes, J. M., & Rodrigues, H. C. (2008). A hierarchical model for concurrent material and topology optimisation of three-dimensional structures. *Structural and Multidisciplinary Optimization*, 35, 107–115.
- Deshpande, V. S., Ashby, M. F., & Fleck, N. A. (2001). Foams: topology bending versus stretching dominated architectures. *Acta Materialia*, 49, 1035–1040.
- Evans, A. G., Hutchinson, J. W., Fleck, N. A., Ashby, M. F., & Wadley, H. N. G. (2001). The topological design of multifunctional cellular metals. *Progress in Materials Science*, 46, 309–327.
- Frenzel, T., Kadic, M., & Wegener, M. (2017). Three-dimensional mechanical metamaterials with a twist. *Science*, 358, 1072–1074.
- Ghayesh, M. H., & Farokhi, H. (2017). Nonlinear mechanics of doubly curved shallow microshells. *International Journal of Engineering Science*, 119, 288–304.
- Ghayesh, M. H., Farokhi, H., Gholipour, A., & Tavallaeinejad, M. (2018). Nonlinear oscillations of functionally graded microplates. *International Journal of Engineering Science*, 122, 56–72.
- Gupta, A., & Talha, M. (2015). Recent development in modeling and analysis of functionally graded materials and structures. *Progress in Aerospace Sciences*, 79, 1–14.
- Hassani, B., & Hinton, E. (1998). A review of homogenization and topology optimization II-analytical and numerical solution of homogenization equations. *Computers & Structures*, 69, 719–738.
- He, J. J., & Kang, Z. (2018). Achieving directional propagation of elastic waves via topology optimization. *Ultrasonics*, 82, 1–10.
- Hentschel, M., Schaferling, M., Duan, X. Y., Giessen, H., & Liu, N. (2017). Chiral plasmonics. *Science Advances*, 3(5), e1602735.
- Huang, X. D., Radman, A., & Xie, Y. M. (2011). Topological design of microstructures of cellular materials for maximum bulk or shear modulus. *Computational Materials Science*, 50, 1861–1870.
- Huang, X. D., & Xie, Y. M. (2010). *Evolutionary topology optimization of continuum structures: Methods and applications*. John Wiley & Sons.
- Jha, D. K., Kant, T., & Singh, R. K. (2013). A critical review of recent research on functionally graded plates. *Composite Structures*, 96, 833–849.
- Lakes, R. (1987). Foam structures with a negative poisson's ratio. *Science*, 235, 1038–1040.
- Lazarov, B. S., & Sigmund, O. (2011). Filters in topology optimization based on Helmholtz-type differential equations. *International Journal for Numerical Methods in Engineering*, 86(6), 765–781.

- Li, H., Luo, Z., Gao, L., & Walker, P. (2018). Topology optimization for functionally graded cellular composites with metamaterials by level sets. *Computer Methods in Applied Mechanics and Engineering*, 328, 340–364.
- Li, H., Luo, Z., Zhang, N., Gao, L., & Brown, T. (2016). Integrated design of cellular composites using a level-set topology optimization method. *Computer Methods in Applied Mechanics and Engineering*, 309, 453–475.
- Lin, Z., Groeber, B., Capasso, F., Rodriguez, A. W., & Loncar, M. (2018). Topology-optimized multilayered metooptics. *Physical Review Applied*, 9(4), 044030.
- Liu, J. K., Gaynor, A. T., Chen, S. K., Kang, Z., Suresh, K., & Takezawa, A. (2018). Current and future trends in topology optimization for additive manufacturing. *Structural and Multidisciplinary Optimization*, 57, 2457–2483.
- Liu, Z. Q., Meyers, M. A., Zhang, Z. F., & Ritchie, R. O. (2017). Functional gradients and heterogeneities in biological materials: Design principles, functions, and bioinspired applications. *Progress in Materials Science*, 88, 467–498.
- Popovich, V. A., Borisov, E. V., Popovich, A. A., Sufiakov, V. S., Masaylo, D. V., & Alzina, L. (2017). Functionally graded Inconel 718 processed by additive manufacturing: Crystallographic texture, anisotropy of microstructure and mechanical properties. *Materials & Design*, 114, 441–449.
- Radman, A., Huang, X., & Xie, Y. M. (2014). Maximizing stiffness of functionally graded materials with prescribed variation of thermal conductivity. *Computational Materials Science*, 82, 457–463.
- Rodrigues, H., Guedes, J. M., & Bendsoe, M. P. (2002). Hierarchical optimization of material and structure. *Structural and Multidisciplinary Optimization*, 24, 1–10.
- Schaeffer, T. A., Jacobsen, A. J., Torrents, A., Sorensen, A. E., Lian, J., & Greer, J. R. (2011). Ultralight metallic microlattices. *Science*, 334, 962–965.
- Sigmund, O. (1994). Materials with prescribed constitutive parameters – an inverse homogenization problem. *International Journal of Solids and Structures*, 31, 2313–2329.
- Sigmund, O., & Torquato, S. (1997). Design of materials with extreme thermal expansion using a three-phase topology optimization method. *Journal of the Mechanics and Physics of Solids*, 45, 1037–1067.
- Spanberg, K. (1987). The method of moving asymptotes – a new method for structural optimization. *International Journal for Numerical Methods in Engineering*, 24, 359–373.
- Thomsen, C. R., Wang, F. W., & Sigmund, O. (2018). Buckling strength topology optimization of 2D periodic materials based on linearized bifurcation analysis. *Computer Methods in Applied Mechanics and Engineering*, 339, 115–136.
- Vogiatzis, P., Chen, S. K., Wang, X., Li, T. T., & Wang, L. F. (2017). Topology optimization of multi-material negative Poisson's ratio metamaterials using a reconciled level set method. *Computer-Aided Design*, 83, 15–32.
- Wang, F. W. (2018). Systematic design of 3D auxetic lattice materials with programmable Poisson's ratio for finite strains. *Journal of the Mechanics and Physics of Solids*, 114, 303–318.
- Wang, M. Y., Wang, X. M., & Guo, D. M. (2003). A level set method for structural topology optimization. *Computer Methods in Applied Mechanics and Engineering*, 192, 227–246.
- Wang, Y. G., & Kang, Z. (2017). Structural shape and topology optimization of cast parts using level set method. *International Journal for Numerical Methods in Engineering*, 111, 1252–1273.
- Wang, Y., Luo, Z., Zhang, N., & Qin, Q. H. (2016). Topological shape optimization of multifunctional tissue engineering scaffolds with level set method. *Structural and Multidisciplinary Optimization*, 54, 333–347.
- Wang, Y. Q., Chen, F. F., & Wang, M. Y. (2017). Concurrent design with connectable graded microstructures. *Computer Methods in Applied Mechanics and Engineering*, 317, 84–101.
- Watts, S., & Tortorelli, D. A. (2017). A geometric projection method for designing three-dimensional open lattices with inverse homogenization. *International Journal for Numerical Methods in Engineering*, 112, 1564–1588.
- Wei, K., Peng, Y., Wang, K. Y., Duan, S. Y., Yang, X. J., & Wen, W. B. (2018). Three dimensional lightweight lattice structures with large positive, zero and negative thermal expansion. *Composite Structures*, 188, 287–296.
- Wu, J., Aage, N., Westermann, R., & Sigmund, O. (2018). Infill optimization for additive manufacturing—approaching bone-like porous structures. *IEEE Transactions on Visualization and Computer Graphics*, 24, 1127–1140.
- Xu, H., & Pasini, D. (2016). Structurally efficient three dimensional metamaterials with controllable thermal expansion. *Scientific Reports*, 6, 34924.
- Yan, J., Cheng, G. D., & Liu, L. (2008). A uniform optimum material based model for concurrent optimization of thermoelastic structures and materials. *International Journal for Simulation and Multidisciplinary Design Optimization*, 2, 259–266.
- Yu, N. F., & Capasso, F. (2014). Flat optics with designer metasurfaces. *Nature Materials*, 13, 139–150.
- Zhang, H. K., Luo, Y. J., & Kang, Z. (2018). Bi-material microstructural design of chiral auxetic metamaterials using topology optimization. *Composite Structures*, 195, 232–248.
- Zhang, W. H., & Sun, S. P. (2006). Scale-related topology optimization of cellular materials and structures. *International Journal for Numerical Methods in Engineering*, 68, 993–1011.
- Zhao, Z. L., Zhou, S., Feng, X. Q., & Xie, Y. M. (2018). On the internal architecture of emergent plants. *Journal of the Mechanics and Physics of Solids*, 119, 224–239.
- Zhou, S. W., & Li, Q. (2008). Microstructural design of connective base cells for functionally graded materials. *Materials Letters*, 62, 4022–4024.
- Zhu, B., Skouras, M., Chen, D., & Matusik, W. (2017). Two-scale topology optimization with microstructures. *ACM Transactions on Graphics*, 36(5), 164 (1–16).
- Zhu, J. H., Zhang, W. H., & Xia, L. (2016). Topology optimization in aircraft and aerospace structures design. *Archives of Computational Methods in Engineering*, 23, 595–622.